Rifting under steam – how rift magmatism triggers methane venting from sedimentary basins

C. Berndt[1], C. Hensen[1], C. Mortera-Gutierrez[2], S. Sarkar[1], S. Geilert[1], M. Schmidt[1], V. Liebetrau[1], R. Kipfer[3,7], F. Scholz[1], M. Doll[4], S. Muff[1], J. Karstens[1], S. Planke[5], S. Petersen[1], C. Böttner[1], W.-C. Chi[6], M. Moser[1], R. Behrendt[1], A. Fiskal[1], M.A. Lever[7], C.-C. Su[8], L. Deng[7], M.S. Brennwald[3], and D. Lizarralde[9]

[1]GEOMAR Helmholtz Centre for Ocean Research Kiel, Wischhofstr. 1-3, 24148 Kiel, Germany

[2]Instituto de Geofísica, UNAM, Circuito Exterior, Cd. Universitaria, Coyoacán, D. F., C. P. 04510, Mexico

[3] Department Water Resources and Drinking Water, Eawag, Überlandstrasse 133, 8600 Dübendorf and Noble Gas Laboratory, Institute of Geochemistry and Petrology, ETH, 8092 Zürich, Switzerland.

[4]Fachbereich Geowissenschaften, Universität Bremen, Leobener Str., 28359 Bremen, Germany

[5]Volcanic Basin Petroleum Research AS, Gaustadalleen 21, 0349 Oslo, Norway

[6]Institute of Earth Sciences, Academia Sinica, 128 Academia Rd, Sec.2, Nangang, Taipei, Taiwan

[7]Department of Environmental Systems Sciences, ETH, Universitätstrasse 16 8092 Zürich, Switzerland

[8]Institute of Oceanography, National Taiwan University, No.1, Sec. 4, Roosevelt Road, Taipei 106 ,Taiwan

[9]Woods Hole Oceanographic Institution, Woods Hole, MA 02543-1050 U.S.A.

ABSTRACT

During opening of a new ocean magma intrudes into the surrounding sedimentary basins. Heat provided by the intrusions matures the host rock creating metamorphic aureoles potentially releasing large amounts of hydrocarbons. These hydrocarbons may migrate to the seafloor in hydrothermal vent complexes in sufficient volumes to trigger global warming, e.g. during the Paleocene Eocene Thermal Maximum (PETM). Mound structures at the top of buried hydrothermal vent complexes observed in seismic data off Norway were previously interpreted as mud volcanoes and the amount of released hydrocarbon was estimated based on this interpretation. Here, we present new geophysical and geochemical data from the Gulf of California suggesting that such mound structures could in fact be edifices constructed by the growth of black-smoker type chimneys rather than mud volcanoes. We have evidence for two buried and one active hydrothermal vent system outside the rift axis. The vent releases several hundred degrees Celsius hot fluids containing abundant methane, mid-ocean-ridge-basalt (MORB)-type helium, and precipitating solids up to 300 m high into the water column. Our observations challenge the idea that methane is emitted slowly from rift-related vents. The association of large amounts of methane with hydrothermal fluids that enter the water column at high pressure and temperature provides an efficient mechanism to transport hydrocarbons into the water column and atmosphere, lending support to the hypothesis that rapid climate change such as during the PETM can be triggered by magmatic intrusions into organic-rich sedimentary basins.

INTRODUCTION

When testing climate models by hind casts for past prominent warming events it has become clear that significant drivers are missing (Panchuk et al., 2008; Carozza et al., 2011). Most striking, the reason for a 5-6°C global warming during the PETM remains elusive, although it is clear that more than 2000 Gt of carbon must have entered the atmosphere within a relatively short time span of a few thousand years (Dickens et al., 1995; Zachos et al., 2001). Light carbon isotope ratios were interpreted to suggest that large amounts of biogenic carbon were released through run-away hydrate dissociation events (Kennett et al., 2000). But recent studies call this interpretation in question (Dickens, 2011; Biastoch et al., 2011). Most alternative explanations are also marred by contradictions with available data (Higgins and Schrag, 2006). This includes the hypothesis of carbon mobilization by magmatic intrusions into carbon-rich continental margin sediments during the opening of the North Atlantic (Svensen et al., 2004), because it is difficult to understand how this process could have injected large amounts of carbon into the atmosphere within a short time.

THE ACTIVE HYDROTHERMAL MOUND IN THE GUAYMAS BASIN

New data acquired in the Guaymas Basin (Fig. 1, S1) support the 'tectonic-magmatic' explanation for warming during the PETM. Our data show a 1050 m-wide and 100 m-high mound located above thick sediments approximately 1 km southeast of the northern rift axis of the Guaymas Basin that is emitting carbon-rich hydrothermal fluids (Fig. 2a). The mound and most of the southern flank of the Guaymas rift valley

are underlain by an approximately 100 m-thick chaotic seismic facies (50 to 150 ms two-way-travel time (TWT)) that is part of a widespread mass transport deposit. In the area of the mound another chaotic and low seismic amplitude seismic facies continues further downward to at least 2900 ms TWT or approximately 200-250 metres below seafloor. We interpret this facies as a conduit for the ascending hydrothermal fluids. At this depth high seismic amplitude reflections extend southward from below the rift axis into the basin. These reflections are likely caused by magmatic intrusions which occur throughout the Guaymas Basin (Lizarralde et al., 2010). The bathymetric data (Fig. 1) also show the trace of a NE-SW striking normal fault that stretches to the mound and is dipping westward (Fig. S2). As it strikes in the same direction as the elongate mound axis it is probable that the shape of the mound is controlled by this fault. An approximately 20 m-thick chaotic seismic facies immediately below the base of the mound may indicate that hydrothermal seepage was initially occurring over a broader area and became more focused once fluid pathways had formed. The up to 30°-steep flanks of the mound suggest a high internal angle of repose of the mound-forming material.

A 2.2 km-long profile of ten heat flow stations across the vent field and a 0.4 km-long profile of five stations along the mound consistently show heat flow values larger than 0.3 W/m². The maximum heat flow on top of the mound is heterogeneous with values exceeding 10 W/m², whereas values below 3W/m^2 were measured only 100 m away from the center (Supplementary Table S1). This heat flow pattern is similar to the heat flow distribution at sediment-free mid ocean ridges (Rona et al., 1996). The strong lateral heat flow variations indicate focused heat transport by hydrothermal fluids within narrow fluid pathways.

Samples recovered from the top of the mound show porous Fe-rich sulfides (Fig. S3) consisting predominantly of a boxwork of pyrrhotite crystals with minor pyrite, and marcasite, and rare Zn- and Cu-sulfides (e.g. sphalerite, chalcopyrite, isocubanite). These are accompanied by a small fraction of non-sulfide minerals (e.g., carbonates, opal-A and secondary Fe-oxyhydroxides). The mineralogy makes the samples from the northern rift axis similar to the massive sulfides recovered from the southern Guaymas Basin (Koski et al., 1985; Peter and Scott, 1988). However, they lack the abundant petroleum found in the southern rift samples. In analogy to black smoker deposits from Escanaba Trough the observed mineral assemblage suggests formation temperatures in the range of 270-330°C (Zierenberg et al., 1993).

TIMING OF HYDROTHERMAL ACTIVITY

A 5m-long gravity core was taken ~500 m away from the hydrothermal vent field (Fig. 3). The upper 4 m of the core consist of organic-rich, hemipelagic diatomaceous clay that is typical for most of Guaymas Basin (Damm et al., 1984). By contrast, the lowermost 1 m of core consists of coarse-grained hydrothermal deposits intercalated with clay lenses suggesting the mound to consist of hydrothermal deposits. Given Pb-210-based sedimentation rates of 0.74 m/kyr inside the hydrothermal vent field (Station 40) and of 0.79 m/kyr just outside the hydrothermal vent field along the Northern Guaymas rift axis (Station 66), the hydrothermal deposits are likely 5 to 6 kyr old. This is a minimum age estimate as older hydrothermal material likely exists below and towards the centre of the vent complex. However, we note that sill intrusions quickly cool off after emplacement (Jamtveit et al., 2004) and even thick

intrusions can only sustain hydrothermal systems for a few kyr. Thus, we infer that the mound structure must have formed during the last 5-10 kyr.

ORIGIN OF THE HYDROTHERMAL FLUIDS

We collected sea water in the vicinity of the hydrothermal field (Fig. 3) with Niskin bottles and measured the dissolved gases with an adapted membrane-inlet mass-spectrometer (MIMS (Mächler et al., 2012)). The water is strongly enriched in helium (He) relative to the atmospheric equilibrium conditions (Fig. S5). At the flanks and the bottom of the rift valley He concentrations are similar to the concentrations found in the southern part of the Guaymas Basin(Lupton, 1979) whereas He in the water just above the active smokers is supersaturated by more than a factor of 4 (Fig. S6). This enrichment indicates that the vent injects He directly into the water column. The injected He is strongly enriched in ^{3}He. The $^{3}He/^{4}He$ ratio ($10.8 \cdot 10^{-6}$, Fig. S6, Tab. S3) agrees with that of excess He from the southern part of the Guaymas Basin (Lupton, 1979) pointing to the same general MORB source, and confirms that water circulation in the Guaymas Basin distributes He-rich water from the black smoker region throughout the basin (Marinone, 2003).

Dissolved concentration of light hydrocarbons determined in water sampled at the smoker field (Fig. 3) by Niskin bottles are highly enriched (factor $\geq 10^{5}$) compared to bottom water concentrations (Tab. S2). Calculated end member concentrations (i.e. CH_4= 6.5 mM; Fig. S7) are similar to that of vent fluids measured in the Southern Guaymas Basin. There, CH_4 generation was related to thermocatalytic degradation of organic matter in sediments intruded by magmatic rocks (CH_4 ~6.3 mM, C1/C2+ ~80)(Welhan and Lupton, 1987). The isotopic composition of methane ($\delta^{13}C$: -39 to -14.9 ‰) at our site also indicates thermogenic methane most likely derived from local

sediments, however, with admixture of isotopically heavy methane (Fig. S8). This is consistent with high enrichment in Rn (Tab. S2). The heaviest $\delta^{13}C$-CH_4 is likely related to an abiogenic methane source derived from water rock interaction (e.g., East Pacific Rise-type methane (Welhan and Lupton, 1987)). The presence of abiogenic hydrocarbon is also supported by the isotopic heavy composition of ethane and propane (McDermott et al., 2015; Proskurowski et al., 2008) (Fig. S9). Although the high-temperature aureole at the sill-sediment contact zone appears to be the plausible source for production of hydrocarbons by hydrothermal alteration of organic matter and abiogenic hydrocarbon release by hydrothermal alteration of magmatic rocks (McDermott et al., 2015), our concentration and isotope data do not exclude ^{13}C-enrichment of methane by (high-temperature) secondary oxidation within the sediments (Pan et al., 2006; Biddle et al., 2012). In fact, the strongest methane input from the smoker vent field exhibits an isotopically light $\delta^{13}C$-trend as it is postulated for the PETM event (Dickens, 2011), and any subsequent methane oxidation product would maintain this signal. We note that isotopically-light carbon of biogenic origin accounts for most of the CH_4 that is emitted from the black smoker field, despite the presence of an isotopically-heavy hydrocarbon source of abiogenic, magmatic origin. Thus, we conclude that magmatic activity acts mainly as the heat source that fosters and triggers CH_4 production and release from the post-rift sediments. While abiogenic methane along with MORB-source fluids is indeed emitted, it amounts only to a minor share of the total liberated CH_4 (mixing ratio: $1 : 10^2 - 10^4$, Fig. S8).

COMPARISON TO MOUND STRUCTURES ON THE NORTH ATLANTIC MARGIN

The Guaymas mound resembles positive relief structures on the Paleocene-Eocene seafloor of the Vøring Basin off mid-Norway that have been interpreted as mud volcanoes previously (Svensen et al., 2004; Aarnes et al., 2015). Although deeply buried, the Norwegian mound structures have similar sizes and internal seismic appearance as the newly discovered active vent structure in the northern Guaymas Basin. The Norwegian mound structures are characterized by a transparent to stratified seismic facies confined by a mostly continuous, low-amplitude seismic reflection (Fig. 2b). The bases of these dome structures also have rugged topography with decreased seismic amplitudes and they overlie zones of disturbed seismic reflections with seismic amplitudes different from their host rocks. These seismic anomalies may indicate sediment alteration during vent activity (Fig. 2b). In addition to similar dimensions, the Norwegian and Guaymas structures both have very steep slopes (Fig. 2c) indicating comparable rheological properties which is uncommon even for the steepest mud volcanoes so far described for marine environments (Pinheiro et al., 2003). Seismic data are never fully conclusive – however, the striking morphological similarity and the location of the structures above seismically imaged fluid pathways indicates that the Guaymas vent may be a suitable analogue for the structures that formed at the beginning of the PETM. This link points to an important role of sediment alteration by ascending hydrothermal fluids and mineral precipitation in the formation of the mounds.

IMPLICATIONS

Hydrothermal systems injecting hot, CH_4- and CO_2-rich fluids high up into the water column are a much more efficient mechanism for releasing large amounts of carbon into the atmosphere than mud volcano-style cold seeps. Such focused ‘hot’ input

198 efficiently bypasses microbial benthic filters that may oxidize much of the CH_4 to the
199 less potent greenhouse gas CO_2. Even more important is the observation that
200 hydrothermal systems can inject CH_4 and CO_2 vigorously several hundred meters
201 high up into the water column. In a shallow marine rift environment such as the North
202 Atlantic volcanic rifted margins during the PETM (Planke et al., 2000), such gas
203 plumes may directly reach the atmosphere. Thus, the new observations support the
204 hypothesis that the PETM was caused by the vigorous and wide spread magmatic
205 systems of the North Atlantic large igneous province (Svensen et al., 2004) rather
206 than by large-scale hydrate dissociation.
207

208 **ACKNOWLEDGMENTS**

209 This work is being funded by the German Ministry of Science and Education (BMBF)
210 through the MAKS project. We thank the master and the crew of research vessel
211 Sonne for their invaluable support during cruise SO241.
212

213 **REFERENCES CITED**

214 Biastoch, A., Treude, T., Rüpke, L.H., Riebesell, U., Roth, C., Burwicz, E.B., Park,
215 W., Latif, M., Böning, C.W., Madec, G., and Wallmann, K., 2011, Rising Arctic
216 Ocean temperatures cause gas hydrate destabilization and ocean acidification:
217 Geophysical Research Letters, v. 38, p. n/a–n/a, doi: 10.1029/2011GL047222.

218 Biddle, J.F., Cardman, Z., Mendlovitz, H., Albert, D.B., Lloyd, K.G., Boetius, A., and
219 Teske, A., 2012, Anaerobic oxidation of methane at different temperature regimes
220 in Guaymas Basin hydrothermal sediments: The ISME Journal, v. 6, p. 1018–
221 1031, doi: 10.1038/ismej.2011.164.

222 Carozza, D.A., Mysak, L.A., and Schmidt, G.A., 2011, Methane and environmental
223 change during the Paleocene-Eocene thermal maximum (PETM): Modeling the
224 PETM onset as a two-stage event: Geophysical Research Letters, v. 38, p. n/a–
225 n/a, doi: 10.1029/2010GL046038.

226 Damm, Von, K.L., Edmond, J.M., Measures, C.I., and Grant, B., 1984, Chemistry of
227 submarine hydrothermal solutions at Guaymas Basin, Gulf of California:
228 Geochimica et Cosmochimica Acta, v. 49, p. 2221–2237, doi: 10.1016/0016-

7037(85)90223-6.

Dickens, G.R., 2011, Down the Rabbit Hole: toward appropriate discussion of methane release from gas hydrate systems during the Paleocene-Eocene thermal maximum and other past hyperthermal events: Climate of the Past, v. 7, p. 831–846, doi: 10.5194/cp-7-831-2011.

Dickens, G.R., O'Neil, J.R., Rea, D.K., and Owen, R.M., 1995, Dissociation of oceanic methane hydrate as a cause of the carbon isotope excursion at the end of the Paleocene: Paleoceanography, v. 10, p. 965–971.

Higgins, J.A., and Schrag, D.P., 2006, Beyond methane: Towards a theory for the Paleocene-Eocene Thermal Maximum: Earth and Planetary Science Letters, v. 245, p. 523–537, doi: 10.1016/j.epsl.2006.03.009.

Welhan, J.A. and Lupton, J.E., 1987, Light Hydrocarbon Gases in Guaymas Basin Hydrothermal Fluids: Thermogenic Versus Abiogenic Origin: AAPG Bulletin, v. 71, p. 215–223, doi: 10.1306/94886d76-1704-11d7-8645000102c1865d.

Jamtveit, B., Svensen, H., Podladchikov, Y.Y., and Planke, S., 2004, Hydrothermal vent complexes associated with sill intrusions in sedimentary basins, *in* Geological Society of London, 9 p. p. 233–241.

Kennett, J.P., Cannariato, K.G., Hendy, I.L., and Behl, R.J., 2000, Carbon Isotopic Evidence for Methane Hydrate Instability During Quaternary Interstadials: Science, v. 288, p. 128–133, doi: 10.1126/science.288.5463.128.

Koski, R.A., Lonsdale, P.F., Shanks, W.C., Berndt, M.E., and Howe, S.S., 1985, Mineralogy and geochemistry of a sediment-hosted hydrothermal sulfide deposit from the Southern Trough of Guaymas Basin, Gulf of California: Journal of Geophysical Research: Solid Earth, v. 90, p. 6695–6707, doi: 10.1029/JB090iB08p06695.

Lizarralde, D., Soule, S.A., Seewald, J.S., and Proskurowski, G., 2010, Carbon release by off-axis magmatism in a young sedimented spreading centre: Nature Geoscience, v. 4, p. 50–54, doi: 10.1038/NGEO1006.

Lupton, J.E., 1979, Helium-3 in the Guaymas Basin: Evidence for injection of mantle volatiles in the Gulf of California: Journal of Geophysical Research: Solid Earth, v. 84, p. 7446–7452, doi: 10.1029/JB084iB13p07446.

Marinone, S.G., 2003, A three-dimensional model of the mean and seasonal circulation of the Gulf of California: Journal of Geophysical Research, v. 108, p. 3325–27, doi: 10.1029/2002JC001720.

Mächler, L., Brennwald, M.S., and Kipfer, R., 2012, Membrane Inlet Mass Spectrometer for the Quasi-Continuous On-Site Analysis of Dissolved Gases in Groundwater: Environmental Science & Technology, v. 46, p. 8288–8296, doi: 10.1021/es3004409.

McDermott, J.M., Seewald, J.S., German, C.R., and Sylva, S.P., 2015, Pathways for abiotic organic synthesis at submarine hydrothermal fields: Proceedings of the

National Academy of Sciences, v. 112, p. 7668–7672, doi: 10.1073/pnas.1506295112.

Pan, C., Yu, L., Liu, J., and Fu, J., 2006, Chemical and carbon isotopic fractionations of gaseous hydrocarbons during abiogenic oxidation: Earth and Planetary Science Letters, v. 246, p. 70–89, doi: 10.1016/j.epsl.2006.04.013.

Panchuk, K., Ridgwell, A., and Kump, L.R., 2008, Sedimentary response to Paleocene-Eocene Thermal Maximum carbon release: A model-data comparison: Geology, v. 36, p. 315–5, doi: 10.1130/G24474A.1.

Peter, J.M., and Scott, S.D., 1988, Mineralogy, composition, and fluid-inclusion microthermometry of seafloor hydrothermal deposits in the southern trough of Guaymas Basin, Gulf of California: Canadian Mineralogist.

Pinheiro, L.M., Ivanov, M.K., Saoutkine, A., Akhmanov, G., Magalhães, V.H., Volkonskaia, A., Monteiro, J.H., Somoza, L., Gardner, J.M., Hamouni, N., and Cunha, M.R., 2003, Mud volcanism in the Gulf of Cadiz: results from the TTR-10 cruise: Marine Geology, v. 195, p. 131–151, doi: 10.1016/S0025-3227(02)00685-0.

Planke, S., Symonds, P.A., Alvestad, E., and Skogseid, J., 2000, Seismic volcanostratigraphy of large-volume basaltic extrusive complexes on rifted margins: Journal of Geophysical Research, v. 105, p. 19–335–19–351.

Proskurowski, G., Lilley, M.D., Seewald, J.S., Früh-Green, G.L., Olson, E.J., Lupton, J.E., Sylva, S.P., and KeLLey, D.S., 2008, Abiogenic Hydrocarbon Production at Lost City Hydrothermal Field: Science, v. 319, p. 604–607, doi: 10.1126/science.1151194.

Rona, P.A., Petersen, S., Becker, K., Herzen, Von, R.P., Hannington, M.D., Herzig, P.M., Naka, J., Lalou, C., and Thompson, G., 1996, Heat flow and mineralogy of TAG Relict High-Temperature Hydrothermal Zones: Mid-Atlantic Ridge 26°N, 45°W: Geophysical Research Letters, v. 23, p. 3507–3510, doi: 10.1029/96gl03257.

Svensen, H., Planke, S., Malthe-Sørenssen, A., Jamtveit, B., Myklebust, R., Eidem, T.R., and Rey, S.S., 2004, Release of methane from a volcanic basin as a mechanism for initial Eocene global warming.: Nature, v. 429, p. 542–545, doi: 10.1038/nature02566.

Zachos, J., Pagani, M., Sloan, L., Thomas, E., and Billups, K., 2001, Trends, Rhythms, and Aberrations in Global Climate 65 Ma to Present: Science, v. 292, p. 686–693, doi: 10.1126/science.1059412.

Zierenberg, R.A., Koski, R.A., Morton, J.L., and Bouse, R.M., 1993, Genesis of massive sulfide deposits on a sediment-covered spreading center, Escanaba Trough, southern Gorda Ridge: Economic Geology, v. 88, p. 2069–2098, doi: 10.2113/gsecongeo.88.8.2069.

309

310

311

312

313 **FIGURE CAPTIONS**

314 Figure 1. The Guaymas Basin is one of the rift basins formed by opening of the Gulf
315 of California in NW-SE direction. The recently discovered black smoker is located
316 just south of the northern rift axis.

317

318 Figure 2. Comparison of the seismic signature of the active black smoker (a) and an
319 extinct structure in the Guaymas (b and c) and extinct structures observed in the
320 Vøring Basin during the opening of the Northeast Atlantic off Norway (d and e).
321 Width (f) and height (g) of the active black smoker in the Guaymas Basin are similar
322 to structures in the Vøring Basin as indicated by the red line in the blue histograms.
323 Green lines, average width and height. MTD, mass transport deposit. CSF, chaotic
324 seismic facies underneath the smoker. Vertical axis on all seismic images shows two
325 way travel time in ms.

326

327 Figure 3. Three-dimensional view of the mound structure discovered in the Guaymas
328 Basin. Station IDs of CTD tracks (green lines), HyBis dives (red lines), gravity core
329 (yellow triangle), and in situ sensor data (pCH_4 (μatm) / pCO_2 (μatm) / temperature
330 (°C)) are labelled.

331

332 Figure 4. Schematic diagram illustrating the processes at the active vent site. The
333 green area indicates under-mature sediments from which organic carbon can be

mobilized by the heat transfer from the magmatic intrusions limiting the depth within which the bulk of the fluids may originate. MTD: Mass transport deposit.

[1]GSA Data Repository item 201Xxxx, including supplementary figures and references as well as additional information on heat flow measurements, geochemical analysis of sediment pore water and water column samples, determination of the sedimentation rate and further seismic information, is available online at www.geosociety.org/pubs/ft20XX.htm, or on request from editing@geosociety.org or Documents Secretary, GSA, P.O. Box 9140, Boulder, CO 80301, USA.

GSA Data Repository Materials

Seafloor temperature measurements

The temperature gradients were measured using a 5 m-long temperature-gradient lance with six miniaturized temperature data loggers (MTL). These loggers measured the temperature at a sampling rate of 1 s with an absolute accuracy of approximately 0.1 K (Pfender and Villinger 2002). The relative temperature resolution is 0.001 K. In addition, at six sites a 5 m-long gravity corer with attached MTLs was used. An additional logger at the top of both instruments measured the bottom water temperature as a reference. All measurements were tilt corrected. The derived temperature data were not corrected for sedimentation and terrain effects.

We have measured the thermal conductivity on recovered core material that was sampled at or close to the depth of the measured temperature positions using the KD2 Pro Needle Probe Instrument. For the samples without a thermal-conductivity

measurement, i.e. those without cores, we assumed a constant thermal conductivity of 0.7 W/m K. The data were processed using the method published by Hartmann and Villinger (2002). This method determines undisturbed sediment temperatures from the observed temperature decays.

Heat flow values were calculated by using Fourier's Law as the product of the temperature gradient and thermal conductivity.

We used Bullard method in which the integrated thermal resistance is plotted as a function of temperature. Usually this relationship is linear. However, transient processes such as high sedimentation rates, seasonal temperature fluctuations, focused advection processes or heat generation may cause non-linear deviations. Fourteen out of the 15 presented heat flow sites show a linear relationship between temperatures as function of integrated thermal resistance. Just one site shows non-linear relation at shallow sediment depth.

We interpret the overall high heat flow values with large lateral variations as a result of hydrothermal fluid movements along narrow pathways. The high temperature gradient (Supplementary Table S1) excludes conductive heat transfer. Conductive heat transfer cannot explain either the large lateral heat flow variations on a spatial scale of 100 m. This indicates that there is rigorous hydrothermal venting. All of the SO241-70 sites show advective components. Three out of these four are interpretable as discharge areas (in the northern and central part of the graben), but the Bullard plot of (Site SO241-70P04) shows a downward concave curve at shallow depth, which may be the result of seawater recharge into the crust before it is being heated up.

Geochemistry

Water samples were taken by using a towed SBE9-CTD rosette device equipped with 11 Niskin bottles (a 10 l) and additional HydroC-pCH_4 and -pCO_2, turbidity, and bottom distance sensors (modified after Schmidt et al., 2015). CTD-Stations VCTD09 (and -10) were towed directly above the hydrothermal vent field in variable distance to seafloor (Fig. 3). However, only VCTD09 data is shown in Table S2 as it exhibit notable inorganic variations of hydrothermal tracers in water masses in 5-20 m distance to seafloor. Niskin bottles were closed when temperature, pCO_2 and turbidity suddenly increased indicating hydrothermal plume anomalies. The Niskin bottles were sub-sampled directly after CTD retrieval for inorganic element chemistry, nutrients, partial pressures of dissolved gases and stable and radio-isotope characteristics (Tab. S2) and water samples were analysed onboard for nutrient concentrations. Sub-samples taken for the analysis of major cations (Na^+, K^+, Li^+, Mg^{2+}, Ca^{2+}, Sr^{2+}, Ba^{2+}) as well as B and Si were measured in the shore-based laboratory at GEOMAR Helmholtz-Centre for Ocean Research by ICP-OES (*http://www.geomar.de/en/research/fb2/fb2-mg/benthic-biogeochemistry/mg-analytik/icp-aes/*). ICP sub-samples were acidified directly after sampling to prevent any precipitation of minerals. The elements Ba, Mn, Si, and Li are enriched compared to seawater values. The concentration ranges between 128 – 1766 nM for Ba, 0.02 to 23.9 µM for Mn, 0.16 – 0.69 mM for Si and 23.1 – 59.2 µM for Li (Table S2). All elements show the strongest anomalies (mostly enrichment) in bottle 12 (VCTD09). Mg shows a slight concentration decrease compared to seawater. The strongest depletion of Mg (51 mM) was also encountered in bottle 12. TIMS measured $^{87}Sr/^{86}Sr$ ratios normalized on SRM-987 (0.710248) ranges between 0.708906 and almost

409 modern seawater (0.709176) matching 0.709170 (± 1 E-5, typical 2 SEM this session)
410 showing the lowest value in bottle 12 which was sampled closest to the active vent.
411
412 We calculated the amount of hydrothermal fluids in the Guaymas Basin bottom water
413 using a simple two-end member mixing model between the seawater and primary
414 hydrothermal fluid which was assumed to be void of Mg. Based on this we calculated
415 the maximum percentage of the hydrothermal fluid in the water samples. The lowest
416 Mg concentration of 51 mM in the water sample of bottle 12 yields a hydrothermal
417 fluid percentage of ~6 %. Based on this we determined the hydrothermal end member
418 composition of the enriched elements in the sampled water column and compared
419 those to the concentrations measured at the southern Guaymas spreading center by
420 Von Damm et al. (1985).
421
422 Hydrothermal end member concentrations for Si and Ba yielded 9.36 mM and 28 µM,
423 respectively and fall well into the end member concentration ranges observed by Von
424 Damm et al. (1985) in the southern Guaymas Basin (Si: 9 - 14 mM; Ba: 7 – 42 µM).
425 Si concentration is at the lower end of the concentration range and might point to a
426 lower hydrothermal temperature or Si precipitation during ascent or after fluid
427 discharge. Hydrothermal end member concentrations calculated for Mn yield 420 µM,
428 which is higher than the concentrations observed in the southern Guaymas
429 hydrothermal fluids, which range between 128 and 236 µM (Von Damm et al., 1985).
430 Von Damm et al. (1985) propose the precipitation of alabandite (MnS) as an
431 explanation for the observed low values. Li, in contrast, shows slightly lower
432 calculated end member concentrations (584 µM) compared to the southern Guaymas
433 fluids, which range between 630 and 1076 µM. These lower values might be

434 explained by a Li sink in the sediments through which the hydrothermal fluids
435 percolate.
436
437 Concentrations of dissolved He and Ne (as well as Ar, Kr and Xe) and the $^{3}He/^{4}He$,
438 $^{22}Ne/^{20}Ne$, $^{36}Ar/^{40}Ar$ isotope ratios in water samples taken in copper tubes were
439 analysed as routine samples in the noble gas laboratory of the Swiss Federal Institute
440 of Technology Zurich (ETHZ) and the Swiss Federal Institute of Aquatic Science and
441 Technology (Eawag). Details on sampling and of the experimental method are given
442 in Beyerle et al. (2000). He and Ne concentrations are covered with an overall
443 standard error of ±2%, the $^{3}He/^{4}He$ ratio has a standard error of 1%.
444
445 For the on-board analysis concentrations of dissolved He, Ar, Kr, N_2, O_2, CO_2, and
446 CH_4 during the expedition, we used a portable gas-equilibrium membrane-inlet mass-
447 spectrometric system (GE-MIMS) similar to that described in Mächler et al. (2012).
448 Whereas the original GE-MIMS was designed for gas analysis in continuous high-
449 volume water flows through a large membrane contactor, the GE-MIMS used here
450 was modified to allow analysis of an 8 l water sample taken from a 10 l Niskin
451 sampler within 10 min (Brennwald et. al., 2015, a, b). To allow reliable gas analysis
452 in this limited amount of water, the gas consumption from the membrane contactor
453 into of the MS was reduced to 0.1 ccSTP/min (> 2 ccSTP/min in the original GE-
454 MIMS). This allowed maintaining gas/water solubility equilibrium in miniature
455 membrane contactor modules (two LiquiCel MicroModules operated in parallel) at a
456 total water throughput of 0.5 L/min (> 5 L/min in the original GE-MIMS). The low
457 gas consumption was achieved by replacing the capillary flow resistance followed by
458 a split-flow/aperture gas inlet to the MS vacuum by a new splitless design using a

459 single capillary (9 m long, 0.1 mm inner diameter, Brennwald et al., 2015b). The gas
460 outflow from the capillary is analysed in a quadrupole MS (Stanford Research
461 Systems RGA 200) operated in dynamic mode. As the membrane contactors operate
462 at solubility equilibrium, the partial pressures of the noble gases N_2 and O_2 in the gas
463 phase of the membrane contactors are similar to those in air. The GE-MIMS data for
464 these species were therefore calibrated using ambient air as a reference gas (< 5 %
465 accuracy, 1 σ). The partial pressures of CO_2 and CH_4 are reported as un-calibrated
466 raw data.
467
468 In order to determine the variation of excess amounts of the noble gas radon
469 ($^{222}Rn_{(exc.)}$) close to the hydrothermal vent, selected CTD samples were measured on
470 board by Liquid Scintillation Counting (LSC). Using a portable Hidex Triathler^{TM}
471 system and MaxiLight^{TM} as scintillation cocktail for the measurement of total ^{222}Rn
472 content uncertainties of 15% (SD) are typical for the counting statistics. After more
473 than 3 months storage re-measurements were conducted at GEOMAR to correct for
474 the fraction of total ^{222}Rn potentially provided by the decay of dissolved ^{226}Ra. The
475 analytical procedure followed the approach described by Purkl and Eisenhauer
476 (2004). The maximum sample size was restricted to 1.5 l combined with 20 ml of
477 LSC cocktail, which is close to the maximum extraction efficiency as recently
478 deduced by Schubert et al. (2014). The re-measurements for supported ^{222}Rn
479 contribution did not reveal concentrations above the detection limit of the applied
480 LSC setup. Consequently, a simple, robust, and reliable semi-quantitative measure on
481 the relative enrichment in $^{222}Rn_{(exc.)}$ can be presented in Tab. S2 in terms of
482 enrichment factors compared to bottle 5. Since bottle 5 shows the lowest ^{222}Rn
483 activity in dpm/L (decay per minute/liter) of the investigated CTD casts it provides

484 the best available approximation to water column background ^{222}Rn activity and was
485 set as reference point (Tab. S2). The lowest published ^{222}Rn data (0.1 and 0.2 dpm/L)
486 of Santos et al. (2011) for central waters of the Concepcion Bay (West of our study
487 area) and of Prol-Ledesma et al. (2013) for the northern Gulf of California (Wagner
488 and Consag basins, down to zero dpm/100L) may be assumed as typical background
489 values and are similar to the lowest values that we have encountered (bottle 5, 1768
490 m: 0.17 dpm/L (± 0.1, SD; calibration pending). However, applying the same
491 approach to the sample recovered closest to the vent (bottle 12, 1773 m) yielded the
492 maximum $^{222}Rn_{(exc.)}$ activity of 13.8 dpm/L for our data set. Independent from exact
493 quantitative setup calibrations, this approach provides a robust enrichment factor for
494 $^{222}Rn_{(exc.)}$ in the same order of magnitude as deduced for He in this study (Tab. S2).
495 However, almost twice as high levels of $^{222}Rn_{(exc.)}$ of 2430 dpm/100L were reported
496 for the hydrothermal impact on the waters of the northern Gulf of California in the
497 Wagner and Consag basins (Prol-Ledema et al., 2013). There they attribute the
498 positive anomalies of ^{222}Rn to a fault system coinciding with the presence of strong
499 flares suggesting hydrothermal circulation in a thick sediment cover and revealing the
500 location of up-flow areas.
501
502 Dissolved hydrocarbons (C1-C3) from individual water samples were released
503 onboard by equilibration of 112 ml water samples in a septum-sealed 117 ml
504 headspace vial at room temperature (He-head space, 50 µl $HgCl_2$-solution added).
505 Hydrocarbon composition of the head space gas was determined by using a Thermo
506 Trace gas chromatograph (GC) equipped with flame ionization detector (carrier gas:
507 He 5.0; capillary column: RT Alumina Bond-KCl, column length: 50 m; column
508 diameter: 0.53 µm). Precision of ±1-3% was achieved when measuring standard

hydrocarbon mixtures. Molar hydrocarbon concentrations in Table S2 were calculated by applying Henry coefficients according to Mackay and Shiu (2006).

Stable carbon isotope ratios of methane and higher hydrocarbons (C1-C3) from water samples were measured by using continuous flow GC combustion - Isotope Ratio Mass Spectrometry. Hydrocarbons were separated in a Thermo Trace GC (carrier gas: He; packed column: ShinCarbon, 1.5 m). The subsequent conversion of hydrocarbons to carbon dioxide was conducted in a Ni/Pt combustion furnace at 1150°C. The $^{13}C/^{12}C$-ratios of the produced CO_2 were determined by a Thermo MAT253 isotope ratio mass spectrometer. All isotope ratios are reported in the δ-notation with respect to Vienna Pee Dee Belemnite (VPDB, analytical precision 0.5 ‰).

Sedimentation Rates

The wet sediment was weighed, freeze dried at -80°C and reweighed to determine the water content, then ground in a mortar. Radionuclides were then measured as follows. Two HPGe detectors were engaged for ^{210}Pb and ^{226}Ra analysis including GMX-type (ORTEC GMX-120265) and well-type (ORTEC GWL-100230) detectors which interfaced to a digital gamma-ray spectrometer (DSPecPlus™). For the GMX-type detector, absolute counting efficiencies for various photon energies were calibrated using IAEA reference materials 327A, 444 spiked soil, CU-2006-03 spiked soil, RGTh and RGU for sample weight at 100g as a reference, and coupled with an in-house secondary standard for various masses (from 10 to 250 g) to calibrate the effect of sample mass on the attenuation of γ-rays of various energies. For the well-type detector, the counting efficiencies were calibrated by IAEA-RGTh and RGU from 0.5 to 3.5 g. ^{214}Pb was used as an index of ^{226}Ra (supported ^{210}Pb) whose activity

concentration was subtracted from that of the measured total ^{210}Pb to obtain excess ^{210}Pb ($^{210}Pb_{ex}$). The ^{210}Pb and ^{214}Pb activities were quantified based on photon peaks centered at 46.52 and 351.99 keV, respectively. The activities of radionuclides were decay-corrected to the date of sample collection. All radionuclide data were calculated on salt-free dry weight basis. Error bars represent ±1σ around the mean based on counting statistics and standard propagation of errors.

Supplementary references not in the main manuscript

Beyerle, U., Aeschbach-Hertig, W., Imboden, D. M., Baur, H., Graf, T., Kipfer, R. (2000) A mass spectrometric system for the analysis of noble gases and tritium from water samples. Env. Sci. Technol., 34, 2042-2050.

Brennwald, M.S., Rüssel, R., Kipfer, R. (2015a) Recent advances in the on-site analysis and process-based interpretation of dissolved (noble) gases in water bodies. Goldschmidt Abstracts, 386.

Brennwald, M.S., Rüssel, R., Kipfer, R. (2015b) Landing (noble) gas analytics in the field: towards real time insitu gas determination. Goldschmidt Abstracts, 387.

Des Marais, D. J., Stallard, M. L., Nehring, N. L. & Truesdell, A.H. Carbon isotope geochemistry of hydrocarbons in Cerro Prieto geothermal field, Baja California Norte, Mexico. *Chemical Geology* **71**, 159–167, 1988.

Hartmann A, Villinger H (2002) Inversion of marine heat flow measurements by expansion of the temperature decay function. *Geophysical Journal International* 148 (3): 628-636. doi:10.1046/j.1365-246X.2002.01600.x

Lupton, J. E. (1979) Helium-3 in the Guaymas Basin: evidence for injection of mantle volatiles in the Golf of California, *Journal of Geophysical Research* 84: 7464.7452.

559 Mackay, D. & Shiu, W. Y. A critical review of Henry's law constants for chemicals
560 of environmental interest. *J. Phys. Chem. Ref. Data* **10** (4), 1175–1199 (2006).
561 Mächler, L., Brennwald, M. S., and Kipfer, R. (2012) Membrane inlet mass
562 spectrometer for the quasi-continuous on-site analysis of dissolved gases in
563 groundwater. *Environmental Science and Technology* 46: 8288-8296.
564 Padilla y Sánchez, R.J., Domínguez Trejo, I., López Azcárraga, A.G., Mota Nieto, J.,
565 Fuentes Menes, A.O., Rosique Naranjo, F., Germán Castelán, E.A., Campos
566 Arriola, S.E., 2013, National Autonomous University of Mexico Tectonic Map of
567 Mexico GIS Project, American Association of Petroleum Geologists GIS Open
568 Files series.
569 Pfender M, Villinger H (2002) Miniaturized data loggers for deep sea sediment
570 temperature gradient measurements. *Marine Geology* 186: 557-570
571 Prol-Ledesma R.M., Torres-Vera M.A., Rodolfo-Metalpa R., Ángeles C., Lechuga
572 Deveze C.H., Villanueva-Estrada R.E., Shumilin E. and Robinson C. (2013) High
573 heat flow and ocean acidification at a nascent rift in the northern Gulf of
574 California. *Nature Communications*, DOI: 10.1038/ncomms2390.
575 Purkl S. and Eisenhauer, A. (2004) Determination of Radium Isotopes and ^{222}Rn in a
576 groundwater affected coastal area of the Baltic Sea and the underlying sub-sea
577 floor aquifer. *Marine Chemistry*, 87 . pp. 137-149.
578 Santos I., Lechuga-Deveze C., Peterson R.N. and Burnett W.C. (2011) Tracing
579 submarine hydrothermal inputs into a coastal bay in Baja California using radon.
580 *Chemical Geology*, 282, pp. 1-10.
581 Schmidt, M., Linke, P., Sommer, S., Esser, D. & Cherednichenko, S. Natural CO_2
582 seeps offshore Panarea – A test site for subsea CO_2 leak detection technology.
583 *Marine Technology Society Journal* **49** (1), 19-30 (2015).

584 Schubert M., Kopitz J. and Chalupnik S. (2014) Sample volume optimization for
585 radon-in-water detection by liquid scintillation counting. *Journal of Environmental*
586 *Radioactivity*, 134, pp. 109-113.
587 Von Damm, K. L., Edmond, J. M., Measures, C. I., Grant, B. (1985) Chemistry of
588 submarine hydrothermal solutions at Guaymas Basin, Gulf of California.
589 *Geochimica Cosmochimica Acta* 49: 2221–2237.

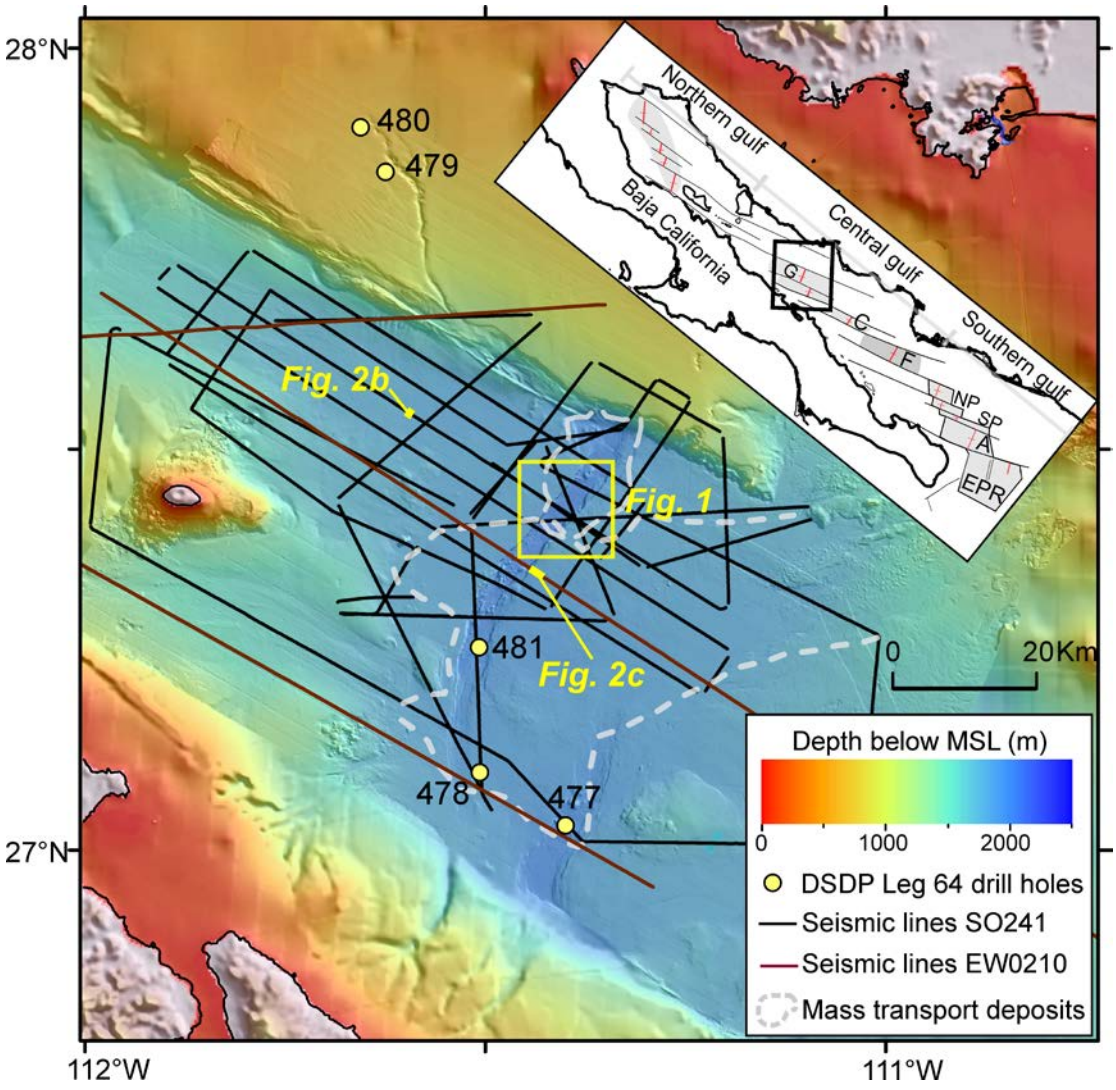

Figure S1: Seismic base map showing the distribution of available 2D seismic data in the Guaymas Basin and major structural elements (after Padilla y Sánchez et al., 2013). Central and Southern gulf spreading centers are labelled, G–Guaymas, C–Carmen, F–Farallon, NP–North Pescadero, SP–South Pescadero, A–Alarcon, EPR–East Pacific Rise.

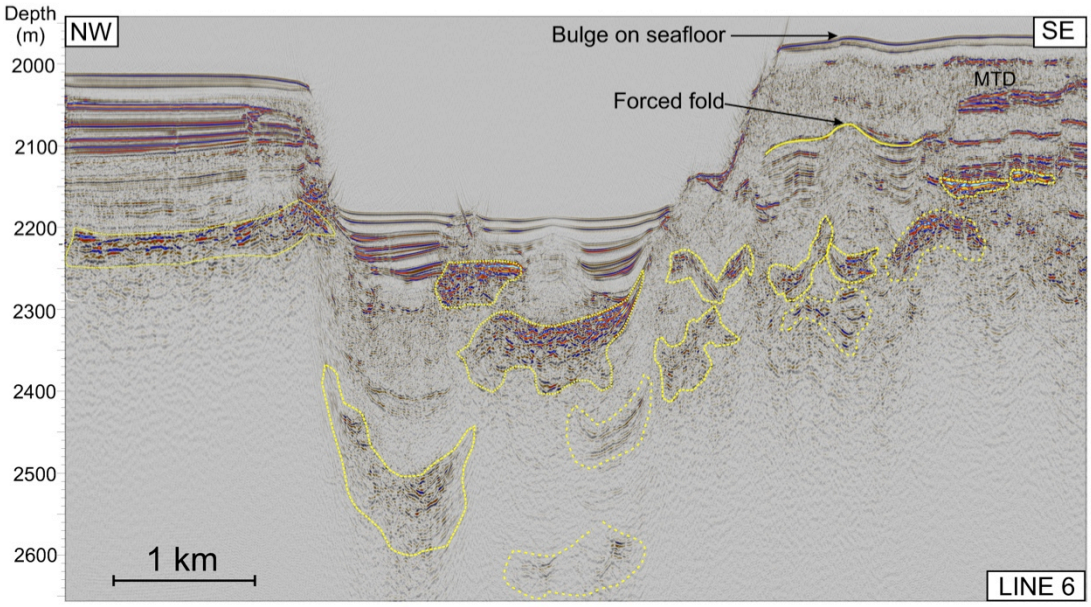

Figure S2: 2D seismic line showing the regional mass transport deposit (MTD) and interpreted sill intrusions (yellow polygons).

Figure S3: Photograph of a massive sulfide sample collected on the southern summit of the mound structure.

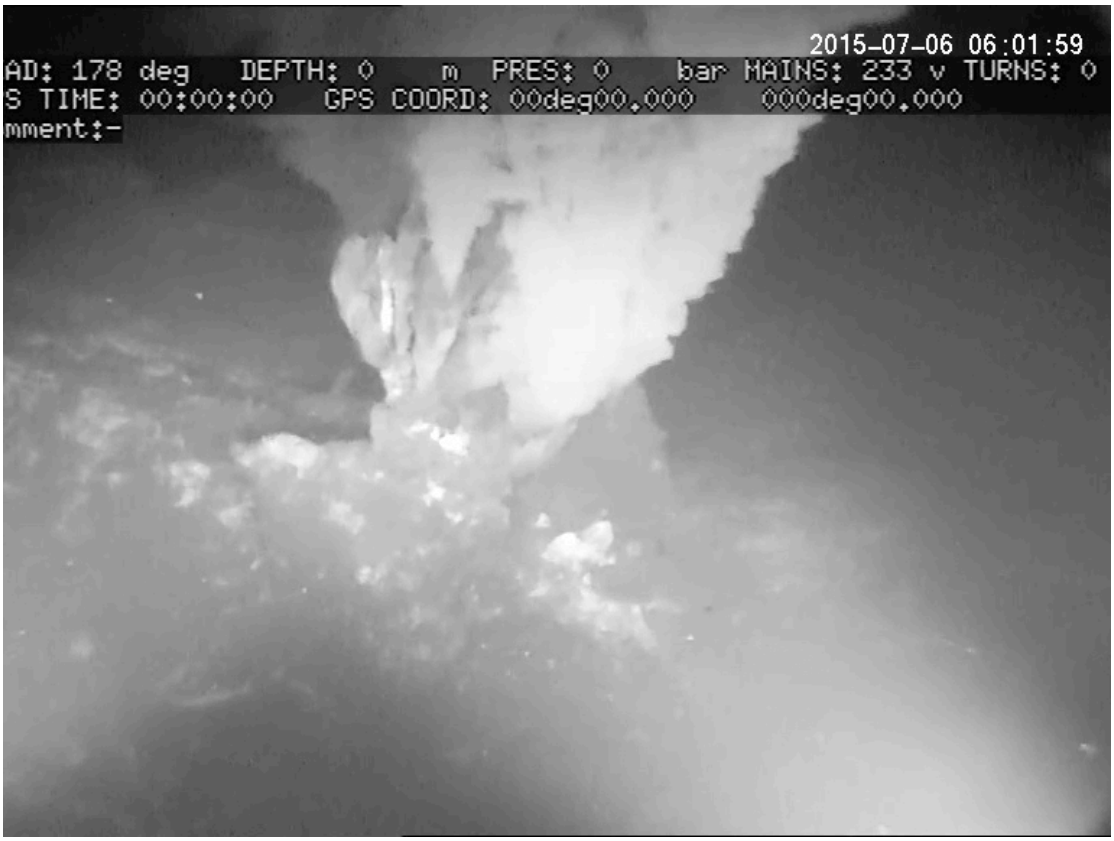

Figure S4: Video still of one of the seven active vents on top of the mound structure.

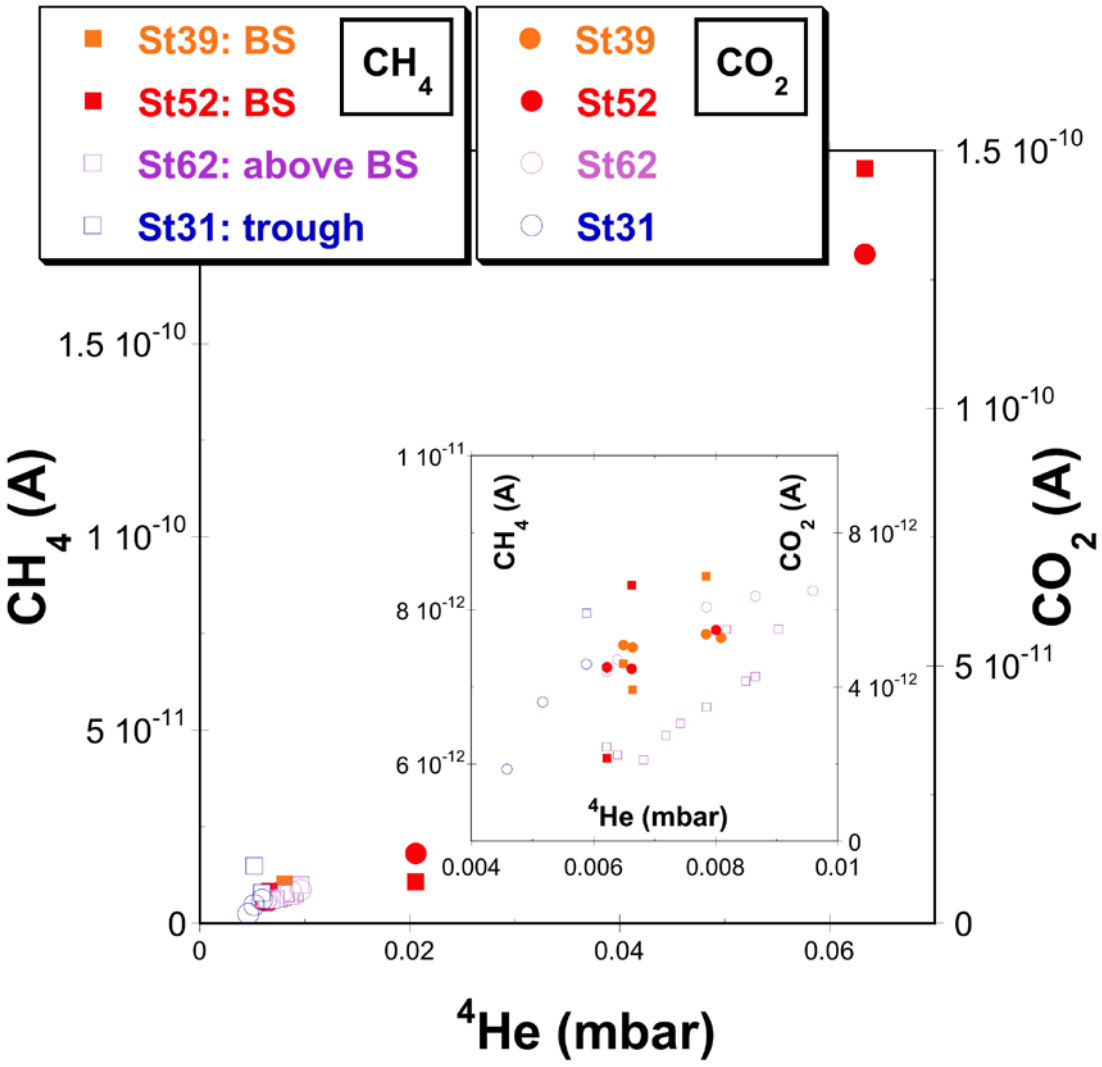

613

614

615 Figure S5: MIMS-determination of dissolved $^{(4)}He$, CH_4 and CO_2 partial pressures

616 (mbar) measured at, above and in the vicinity of the hydrothermal vent site (Stxy:

617 station number xy, BS: 'Black Smoker - within the hydrothermal field (stations: 39,

618 52)', above BS: 'free water column above vent sites (station 62)', trough: samples in

619 the deep trough of the northern Guaymas Basin (station 31)).

620 The partial pressures of CO_2 and CH_4 are reported as un-calibrated raw MIMS

621 detector signals.

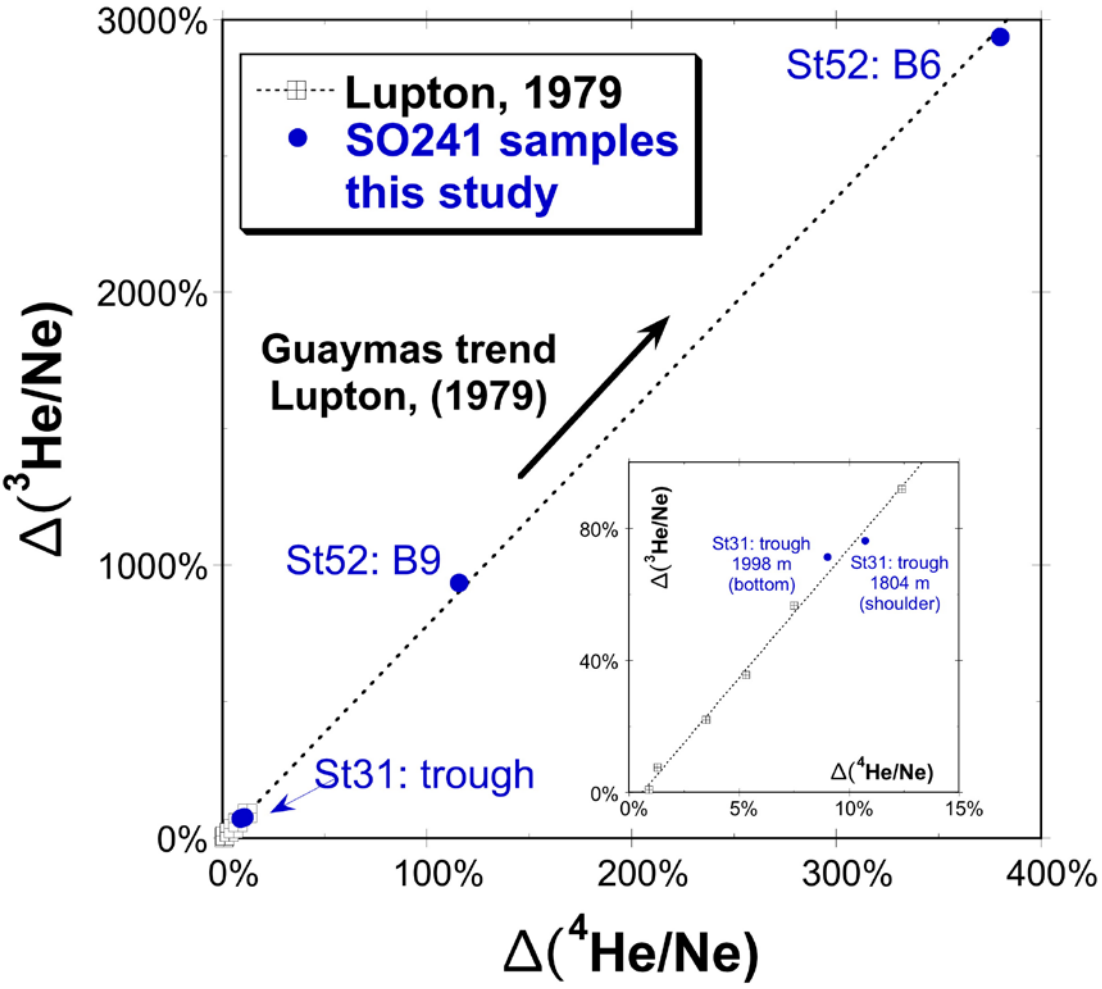

Figure S6: Dissolved He and Ne concentrations measured at the hydrothermal vent site in comparison to earlier noble gas measurements in the southern part of the Guaymas Basin (Lupton, 1979). The samples from the vent site fall on the line defined by the earlier measurements from the southern Guaymas Basin and thus carry isotopic light He ($^3He/^4He$: $10.8 \cdot 10^{-6}$, Lupton, 1979) from the same general MORB source. For comparison noble gas (isotope) concentrations are reported and normalized as in Lupton, 1979:

$$\Delta\left(\frac{^{i}He}{Ne}\right)=\left(\frac{^{i}He_m}{Ne_m}\times\frac{He_{ASW}}{Ne_{ASW}}-1\right)\times 100\ \%$$

633

634 where X_m depicts the measured concentration of X, and X_{ASW} is the expected
635 atmospheric equilibrium concentration (atmospheric saturated water: ASW) for the
636 given physical condition of the water. As $^{i}He_{ASW}$ and Ne_{ASW} only barely change with
637 varying temperature and salinity the $Ne_{ASW}/^{i}He_{ASW}$ ratio is virtually independent of
638 the actual physical condition of the water. Stxy: 'station number, 'Bz': bottle number.
639 Station 52: Black Smoker site, Station 31: open water column of the trough.

640

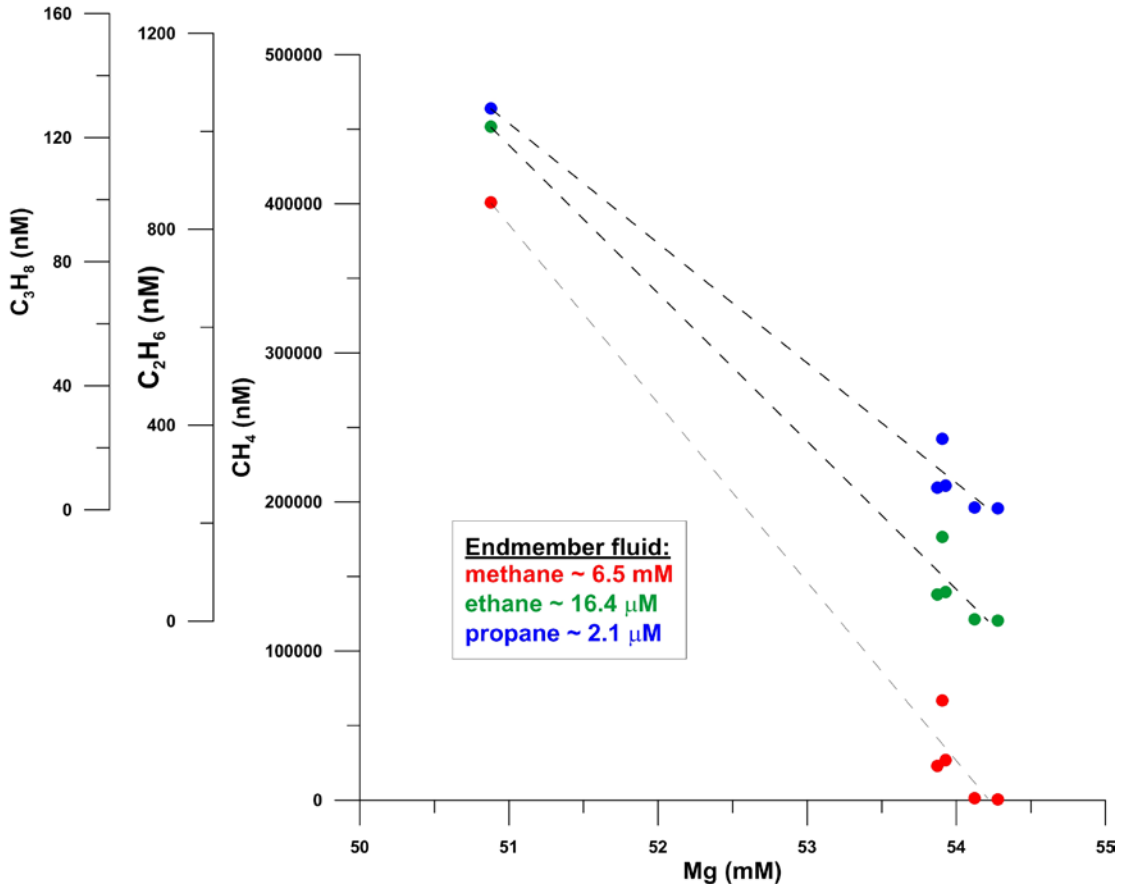

641

642

643 Figure S7: Hydrocarbon end member concentrations (methane, ethane, propane)

644 calculated for hydrothermal fluids venting at the smoker area.

645

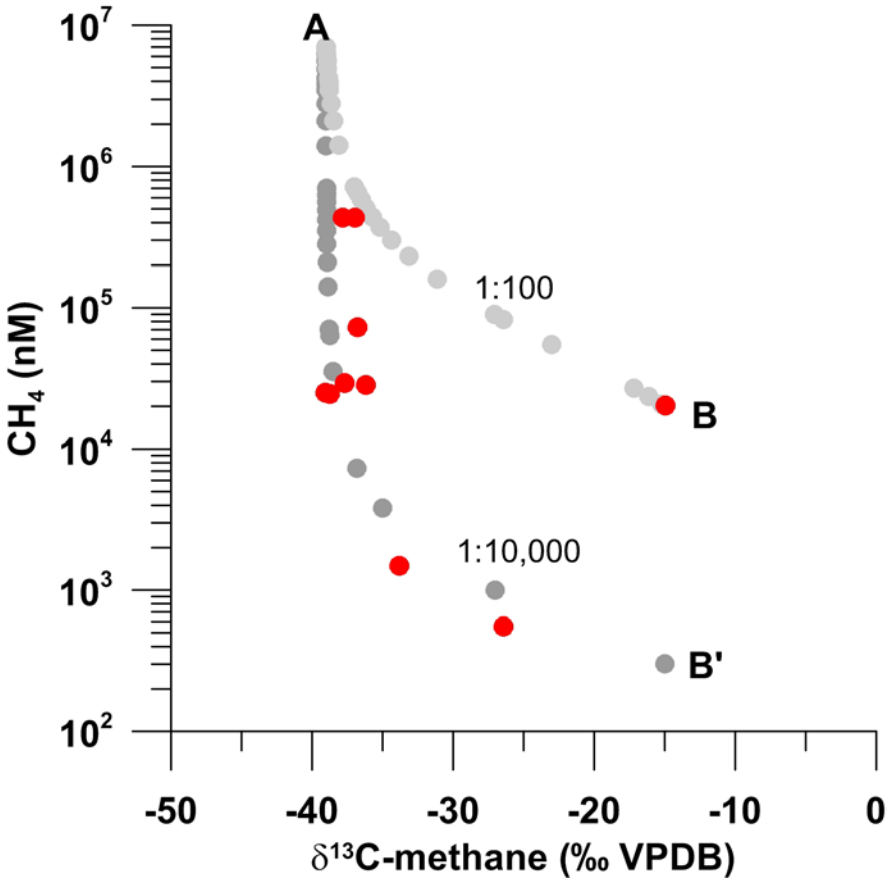

Figure S8: Dissolved methane concentration and carbon isotope data (red dots) determined in bottom water samples from the smoker area. Grey dots indicate mixing curves of a hydrothermal end member methane A (δ^{13}C =-39 ‰, 7nM) with admixture of a second methane-containing fluid B and B' (δ^{13}C =-15 ‰), respectively, at variable dilution factors of 1:100 and 1:10,000 compared to fluid A.

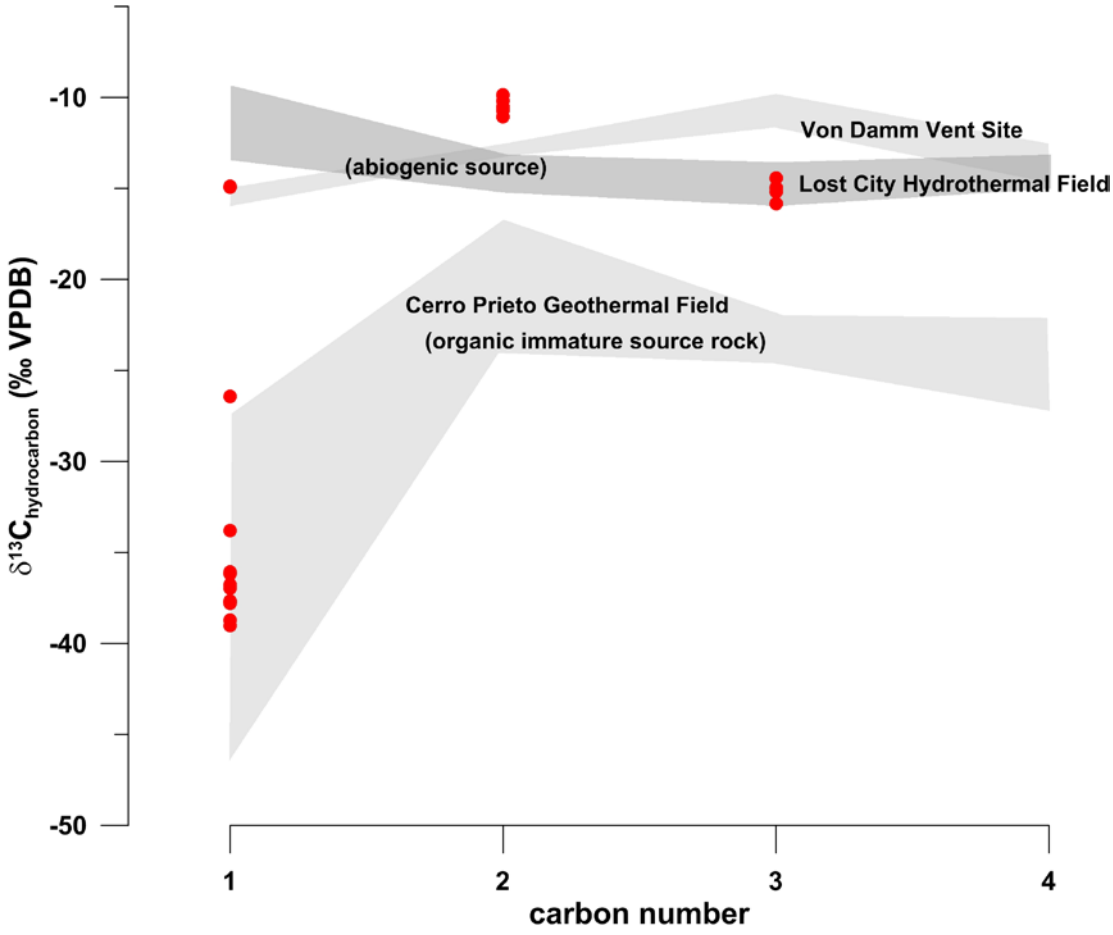

Figure S9: Stable carbon isotope composition of hydrocarbons dissolved in venting hydrothermal fluids (red dots) indicate both hydrocarbons derived from organic matter degradation influenced by volcanic heat intrusion (e.g. Cerro Prieto volcanic complex; Des Marais, 1988), and abiogenic hydrocarbon formation (e.g. Lost City HF, Proskurowski et al., 2008; Von Damm Vent, McDermott et al., 2015).

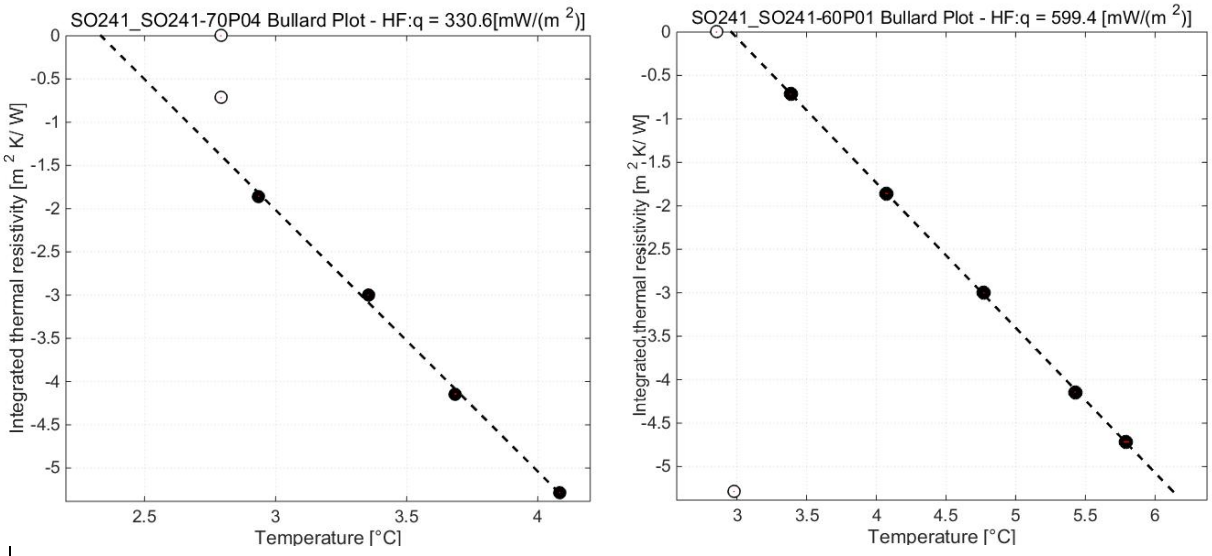

662

663 Figure S10: Calculated heat flow for Site SO241-70P04 (top) and SO241-60P01

664 (bottom) using the Bullard Plot method. Black dots represent sensors used to calculate

665 the heat flow whereas unfilled dots represent the sensor positions, which were not

666 used for any calculations because they were affected by surface artifacts such as

667 incomplete penetration of the lance.

668

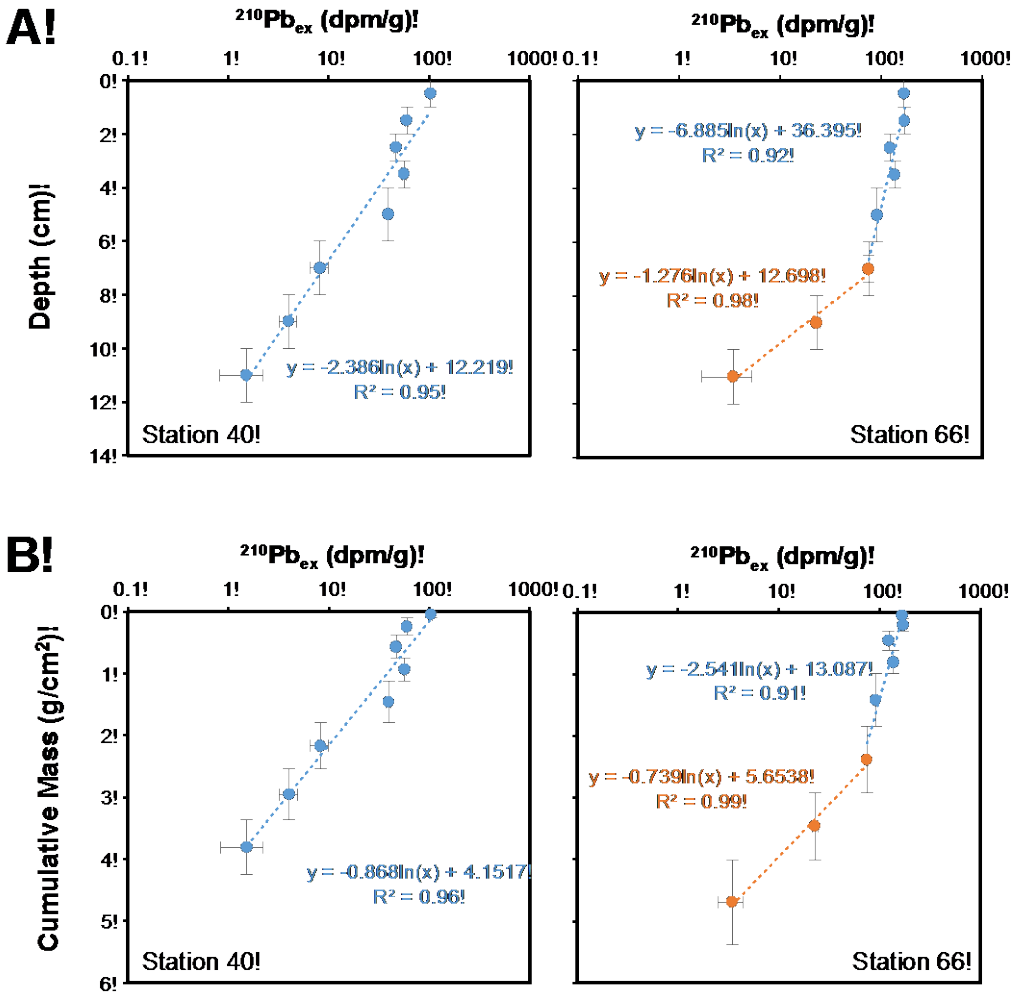

Figure S11: $^{210}Pb_{ex}$ values plotted versus (A) sediment depth and (B) cumulative mass at Stations 40 and 66. Lines and equations represent linear-best fit functions and their data fit (R^2). Station 40 has a good linear fit from the surface to the deepest layers sampled, indicating a relatively steady sedimentation rate over the sampling interval. By contrast, Station 66 has two best-fit lines, one to match samples from the top 6 cm (cyan), and a second one to match samples from 6-12 cm (orange). Samples from the top 6 cm at Station 66 show an only minor decrease in $^{210}Pb_{ex}$, presumably due to vertical sediment mixing by macrofauna. The samples from 6-12 cm at Station 66 show a stronger $^{210}Pb_{ex}$ decrease with depth that more likely reflect the sedimentation rate of the site and were thus used for calculations of sedimentation

681 rates. While the profiles of $^{210}Pb_{ex}$ show good agreement independent of the y-axis
682 units at Station 40, there is a considerable difference between $^{210}Pb_{ex}$ profiles at
683 Station 66 depending on whether sediment depth or cumulative mass are used as y-
684 axis units. This discrepancy is likely an artefact of core compaction during sediment
685 sampling. We consider $^{210}Pb_{ex}$ relationships with cumulative mass, which correct for
686 compaction effects during coring, to be more reliable (especially at Station 66), and
687 thus report sedimentation rates that have been corrected for cumulative mass in this
688 article.

689 ***Supplementary Tables***

690 Table S1: Heat flow measurements carried out during SO241

691

Station	Penetration	Latitude	Longitude	Water Depth [m]	Temp. Gradient [K/m]	k [W/mK]	Heat flow [mW/m²]
SO241-51	Pen 01	27° 24.472'	111° 23.377'	1840	11.441	0.739	8069.3
SO241-58	Pen 01	27° 24.487'	111° 23.377'	1837	9.857	0.720	6508.7
SO241-60a	Pen 01	27° 24.623'	111° 23.626'	1834	0.856	0.7 *	599.4
	Pen 02	27° 24.554'	111° 23.512'	1840	2.789	0.7 *	1952.6
	Pen 03	27° 24.273'	111° 23.396'	1840	4.581	0.7 *	3206.1
	Pen 04	27° 24.408'	111° 23.288'	1849	2.039	0.7 *	1427.0
	Pen 05	27° 24.341'	111° 23.177'	1852	1.014	0.7 *	709.6
	Pen 06	27° 24.265'	111° 23.082'	1844	0.737	0.7 *	516.1
	Pen 07	27° 24.193'	111° 22.956'	1834	0.827	0.7 *	578.7
SO241-60b	Pen 01	27° 24.605'	111° 23.317'	1837	0.391	0.7 *	274.0
	Pen 02	27° 24.552'	111° 23.347'	1834	3.451	0.7 *	2415.4
	Pen 04	27° 24.543'	111° 23.351'	1837	15.479	0.7 *	10835.0
SO241-70	Pen01	27° 25.802'	111° 25.486'	1870	0.375	0.7 *	262.2
	Pen02	27° 25.460'	111° 24.946'	2019	0.483	0.7 *	338.1
	Pen03	27° 25.955'	111° 24.493'	2046	0.432	0.7 *	302.6
	Pen 04	27° 24.837'	111° 23.951	2025	0.457	0.7 *	319.7

Thermal conductivities k with an asterix (*) are assumed.

692

Table S2: Geochemical data of the water column sampled above the black smoker

Bottle	Latitude	Longitude	Depth	Temperature	Salinity	Methane (C1)	Ethane (C2)	Propane (C3)	δ^{13}C-C1	δ^{13}C-C2	δ^{13}C-C3	$^{222}Rn_{(exc.)}$[a]	Mn	Mg	Sr	$^{87}Sr/^{86}Sr$	Si	Ba	Li
	N	W	(m)	(°C)	(‰)	(nM)	(nM)	(nM)	(‰ VPDB)	(‰ VPDB)	(‰ VPDB)	enrich. fact.	(µmol/l)	(mmol/l)	(µmol/l)		(mmol/l)	(nmol/l)	(µmol/l)
1	27.41258	-111.3870	1504	3.1	34.60														
2	27.41284	-111.38696	1766	2.9	34.61	1366.1	3.7	0.8	-33.8				0.02	53.0	88.6		0.16	128	23.1
3	27.41288	-111.38696	1767	2.9	34.61							1.7	<d.l.	54.1	88.7	0.709170	0.18	145	24.9
4	27.41204	-111.38732	1768	4.1	34.55	508.2	0.8	0.4	-26.4				0.14	52.8	88.2		0.18	147	23.3
5	27.41204	-111.38732	1768	4.1	34.64							1.0	<d.l.	54.3	89.2	0.709167	0.18	143	24.9
6	27.4121	-111.38732	1768	4.3	34.68	66885.7	171.7	22.9	-36.8	-9.9	-15.8		0.49	52.9	88.4		0.18	451	23.8
8	27.4121	-111.38732	1768	4.4	34.62							16.2	3.79	53.9	89.6	0.709129	0.26	946	29.0
9	27.41212	-111.38734	1772	6.9	34.64	26801.6 26010.5	59.1 57.4	7.8 8.2	-37.7 -36.2	-10.5			1.33	53.9	88.6	0.709156	0.20	410	26.5
10	27.41214	-111.3872	1775	17.4	34.96	22987.6 22466.2	54.2 52.1	7.1 6.8	-39.0 -38.7	-11.1		4.5	1.18	53.9	88.9	0.709159	0.20	383	26.3
11	27.41214	-111.3872	1775	28.0	34.17	18684.1	42.6	6.1	-14.9 -14.9	-10.7	-14.4		1.10[b]	52.9[b]	88.3[b]		0.19[b]	353[b]	24.7[b]
12	27.41212	-111.38718	1773	12.1	34.26	360284.0 400801.8	849.3 893.0 1009.3	137.4 110.2 129.4	-37.0 -37.8	-10.2	-15.0	81.5	23.9	51.0	90.6	0.708906	0.69	1766	59.2

[a]Enrichment factor of ^{222}Rn relative to the lowest value measured on this CTD station (bottle 5). See text for details.

[b]Inorganic geochemistry values are a mixture of bottle 10 (~20%) and bottle 11 (~80%)

Table S3: Isotope ratios of He and Ne reported as the percentage deviations of ^{3}He/Ne and ^{4}He/Ne from the solubility ratios (see Lupton (1979) for details).

Location	Bottle	Latitude	Longitude	Δ(^{3}He/Ne) [%]	Δ(^{4}He/Ne) [%]
		N	W		
Black Smoker	6	27.4121	-111.38732	2937	380
Black Smoker	9	27.41212	-111.38734	936	116
Background trough bottom	2	37.30207	-111.52433	71	9
Background trough shoulder	7	37.30207	-111.52433	76	11